Optical design of the SPIRE instrument for FIRST

Kjetil Dohlen[*a], Alain Origné[a], Dominique Pouliquen[a], Bruce Swinyard[b]

[a]Laboratoire d'Astrophysique de Marseille, 2 Place Leverrier, 13248 Marseille, Cedex 4, France
[b]Rutherford Appleton Laboratory, Chilton, Didcot, OX11 0QX, UK

ABSTRACT

The SPIRE instrument covers the 200-670 micron spectral range with a three-band, 4′ x 8′ diffraction limited field of view photometer, and a dual-band, 2.6′ diameter field of view imaging FTS. Optimisation of the photometer optics has been given a high priority in the instrument design, allowing an all-reflecting configuration with seven mirrors in one plane. The design corrects for the large tilt of the telescope focal plane due to the off-axis position of the SPIRE field of view, and provides two pupil images (where a beam steering mirror and a cold stop are located) and two field images (where a pick-off mirror for the spectrometer and the final image are located). A large back-focal length allows for dichroic band separators and beam folding mirrors. The spectrometer is a Mach-Zehnder-type, dual channel FTS providing two input and two output ports. The output ports are physically separated from the input ports, and the second input port is fed from a black-body source providing compensation of the telescope background, required to minimize the effect of jitter noise. Powered mirrors are used within the interferometer arms to minimize beam diameters and to leave maximum space for the scan mechanism. The complementary output ports are filtered by band-pass filters to provide the two spectral channels required.

Keywords: Optical design, sub-millimeter instrumentation, imaging FTS

1. INTRODUCTION

SPIRE (Spectral and Photometric Imaging REceiver) [1] is designed and optimized for two of the most important scientific goals of the FIRST (Far Infrared Space Telescope) mission: high-z galaxy survey and early phases of star formation. Based on bolometer detectors, the instrument covers the 200-670 μm spectral range, a range which is of particular importance for determining the history of star formation in galaxies and the early stages of star formation in the interstellar medium. Separated into two parts, the instrument incorporates a three-band photometric camera with a 4′ x 8′ field of view (FOV) designed for deep surveys, and a dual-channel imaging Fourier transform spectrometer (FTS) with a 2.6' diameter circular FOV and a nominal resolving power variable from 20 through to 1000.

Optical design of SPIRE is challenging because of several factors. First, the wavelength is large compared with the size of the optical components. Diffraction effects are therefore considerable and the validity of a geometrical optics design approach must continuously be questioned [2]. Second, all optical and mechanical parts warmer than a few kelvin are highly self-luminous at these wavelengths and easily outshine the faint astronomical sources observed. Stray light control is therefore of great importance. While baffling strategy is not part of the present paper, we note that the optical design reflects its needs by providing sufficient space around beams for baffles and oversized mirrors. Third, great importance is attached to the internal instrument aperture stop, the cold stop (CS) and its alignment with the telescope pupil, located at the telescope secondary mirror (M2). This concerns both stability of the pupil position over the FOV (i.e., pupil aberrations), and external and internal instrument alignment. Fourth, low-order design constraints including location of pupil images and intermediate focal planes, as well as focal plane tilt and focal ratio impose a strict set of design rules. The SYNOPSYS optical design program [3] with its flexible macro programming capability and excellent optimization routine has been of great help during the design and characterization of the instrument.

In the following sections we present optical design and image quality of the photometer (Sec. 2) and of the spectrometer (Sec. 3). Sec. 4 discusses the alignment strategy for the instrument and Sec. 5 summarizes the main conclusions of the study.

[*] Correspondence: Email: dohlen@observatoire.cnrs-mrs.fr; WWW: http://www-obs.cnrs-mrs.fr/;
Telephone: +33 (0) 4 95 04 41 24; Fax: +33 (0) 4 91 62 11 90

2. PHOTOMETER OPTICAL DESIGN

The 3.5 m FIRST telescope is a Ritchey-Crétien system and provides a well-corrected image at a focal ratio of F/8.68. Mainly due to the low focal ratio of the primary mirror (F/0.5), the telescope focal surface is highly curved. SPIRE uses an off-axis part of the telescope FOV and its object surface is therefore tilted with respect to the central (gut) ray. Figure 1 shows the FIRST telescope with, to scale, the SPIRE photometer.

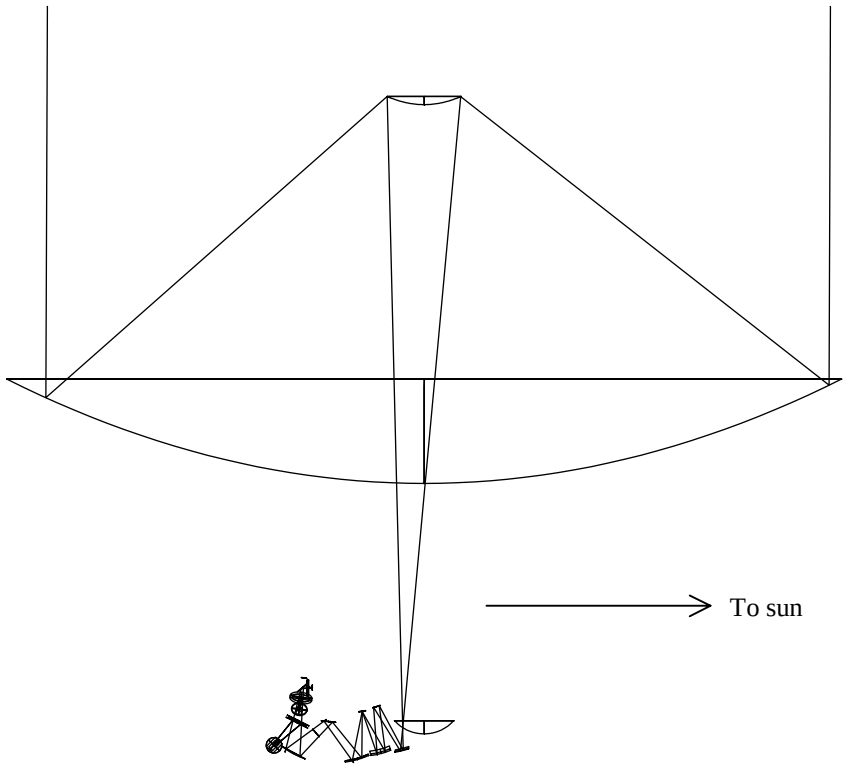

Figure 1. Ray diagram of the FIRST telescope with the SPIRE instrument to the same scale. The primary mirror has a diameter of 3.5 m and the SPIRE instrument is about 500 mm wide.

The functions of the SPIRE photometer optics are to provide:
1) a well-corrected, flat focal surface, perpendicular to the gut ray, at F/5,
2) sufficient back-focal length (BFL) to allow separation of the beam into three spectral bands using dichroics,
3) a well-corrected pupil image near the final focus for the cold stop,
4) an intermediate focal plane to pick off the spectrometer beam, and
5) a pupil image appropriate for chopping and beam steering.

All these functions are assured by the SPIRE optical design as shown in Fig. 2. M3 is an off-axis ellipsoid projecting an image of the telescope secondary (M2) onto M4. This image is well-corrected and in focus at the centre of the M4 so that the pupil image at the cold stop stays fixed during chopping and beam steering. M4 is a flat mirror whose orientation is adjustable in flight to permit ±2′ chopping in the sagittal plane, allowing off-field chopping for a 4′ x 4′ sub-field, and ±30″ beam steering motion in both the tangential and sagittal planes to obtain fully Nyquist sampled images. The toric M5 mirror reimages the focal plane onto M6. While M3 and M4 are common for both photometer and spectrometer, the two systems separate at M6. The photometer M6 is toric and sends the beam into an Offner-type relay system consisting of three spherical mirrors: M7 (concave), M8 (convex), and M9 (concave). Tilt angles, separations and curvatures of these mirrors provide enough free variables to satisfy the three first functions of the above list. In particular, an easily accessible pupil

image is provided between M8 and M9 in which the cold stop is located and which materializes the separation between the 4K cavity surrounding the entire instrument and the 2K cavity (cold box, CB) to which the detectors are bolted.

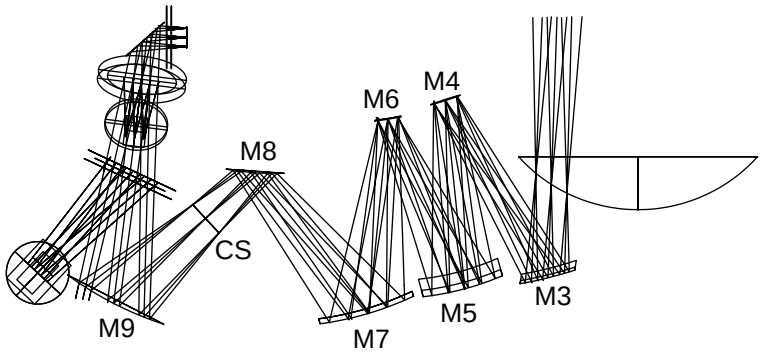

Figure 2. Ray diagram of the SPIRE instrument showing the ray paths for three points in the tangential plane, centre and extremes of the FOV (±2′).

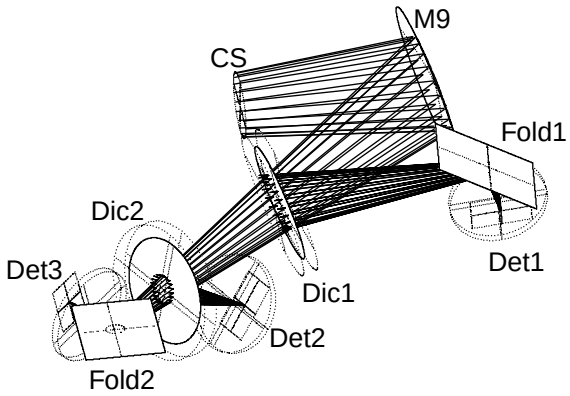

Figure 3. 3D ray diagram of the beam folding within the SPIRE cold box. Det1, Det2 and Det3 are long, medium and short wavelength detector arrays, respectively.

The cold box contains M9, the last powered mirror of the optical train, and dichroics and beam folding mirrors distributing the light between three detector arrays, covering the short (200-300 µm), medium (300-400 µm) and long (400-670 µm) wavelength bands. An edge filter at the cold stop minimizes stray radiation entering the cold box and band-pass filters in front of each detector array ensures the spectral limitation of each band. Figure 3 shows a 3D view of the cold-box optics.

Figure 4 shows geometrical spot diagrams across the photometer FOV. The final focal surface is flat and perpendicular to the gut ray, and the exit pupil is close to telecentric. With a theoretical Strehl ratio better than 0.986 at 250 µm, the system leaves headroom for manufacturing tolerances, and with a distortion below 1.1%, the 10% scientific requirement is met with good margin.

In this instrument, pupil quality is more critical than image quality. An undersized pupil is essential to ensure that the detectors do not see beyond the secondary mirror and so do not receive any emission from warm high-emissivity elements of the cryostat, the telescope and the spacecraft environment. There is a trade-off between stray light rejection and throughput because undersizing means some loss of telescope collecting area. We will come back to the implications of this requirement on instrument alignment in Sec. 4, here we consider the effects of pupil aberrations.

Pupil aberrations quantify the way in which the pupil image moves and distorts at the cold stop as seen from different points in the FOV. The present system has enough free variables to offers good control of these aberrations. Essentially, the conic constant of M3 corrects pupil coma and the toricity of M6 corrects pupil astigmatism, but a general optimization, simultaneously optimizing both pupil and image quality as well as focal length and several geometric constraints, was required for optimal balance of residual aberrations. Figure 5 shows pupil spot diagrams, a graphical presentation of pupil aberrations found most useful in the design work. With a relative pupil displacement $\Delta R/R < 5\%$, the relative loss of collector area for an undersized pupil is $\Delta A/A < 10\%$, where:

$$\Delta A/A = (2 \pi R \Delta R)/(\pi R^2) = 2 \Delta R/R. \quad (1)$$

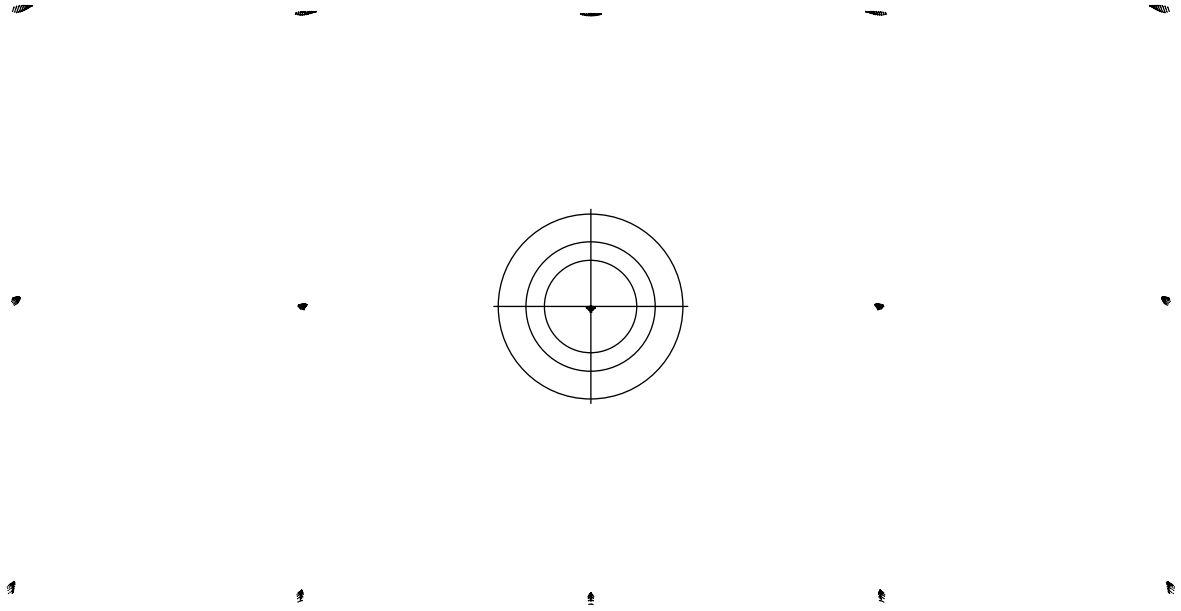

Figure 4. Geometric spot diagrams across the 4′ x 8′ SPIRE photometer FOV. The spots are plotted in their actual positions and to scale. The concentric circles around the central spot have diameters 3.0, 4.3, and 6.1 mm and indicate the Airy disk size at 250, 350, and 500 µm, respectively. With a maximum RMS wavefront error of 4.7 µm, the theoretical Strehl ratio is better than 0.99 anywhere in the FOV at 250 µm. A slight distortion is observed, corresponding to 6″ or 1.1% of the FOV diagonal. The average focal ratio is F/4.9.

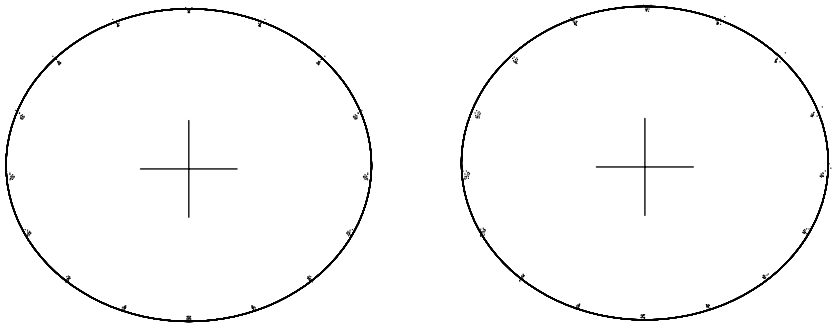

Figure 5. Pupil spot diagrams obtained by tracing rays from 15 positions in the FOV (see Fig. 4) through 16 points along the rim of the telescope pupil to the cold stop. In (a) the M4 beam-steering mirror in its neutral position, in (b) it is tilted by 2.17°, changing the instrument pointing by 2′ in the sagittal plane. Note the oval shape of the cold-stop pupil image. Assuming the nominal M2 image to run through the centre of gravity of each spot, we may measure the radial pupil error ΔR for each point in the FOV at each point along the pupil edge. A useful measure of pupil aberration is relative pupil displacement $\Delta R/R$, found to be less than 5% both in the chopped and unchopped configuration.

3. SPECTROMETER DESIGN

An imaging FTS has been favoured for SPIRE rather than a grating-based solutions because of its superior imaging capability, lower stray-light sensitivity, and variable spectral resolution [4]. Among a large number of possible interferometer concepts, three were chosen for a final comparison, see Figure 6. In each case, two separate, band-limited detector arrays are required to divide the 200-670 µm band into two sub-bands: 200-300 µm, and 300-670 µm. Covering the entire spectrum with a single array would be too constraining with respect to sampling and detection efficiency.

The Martin-Puplett interferometer [5] (Fig. 6 a) offers a good and robust solution to this problem. Based on the use of three polarizers, components which can provide excellent efficiency over a broad band in the far infrared region, and roof-top mirrors, it provides two input and two output ports with a minimum of complexity. When the polarizers are properly oriented, the roof-top mirrors switch the polarization of the beams so that 100% of the light incident upon P2 is transmitted towards the detectors. One polarization of the incident light is lost at P1 however, reducing the optimal efficiency of this concept to 50%. P3 is required to analyze the interfering beams, sending complementary interferograms towards the two detectors. Usually, both detectors would see the entire band, hence detecting all the light incident onto P3, but in our case the spectrum would have to be divided into two by band-pass filtering each detector. This loses another 50%, reducing the theoretical efficiency to 25%.

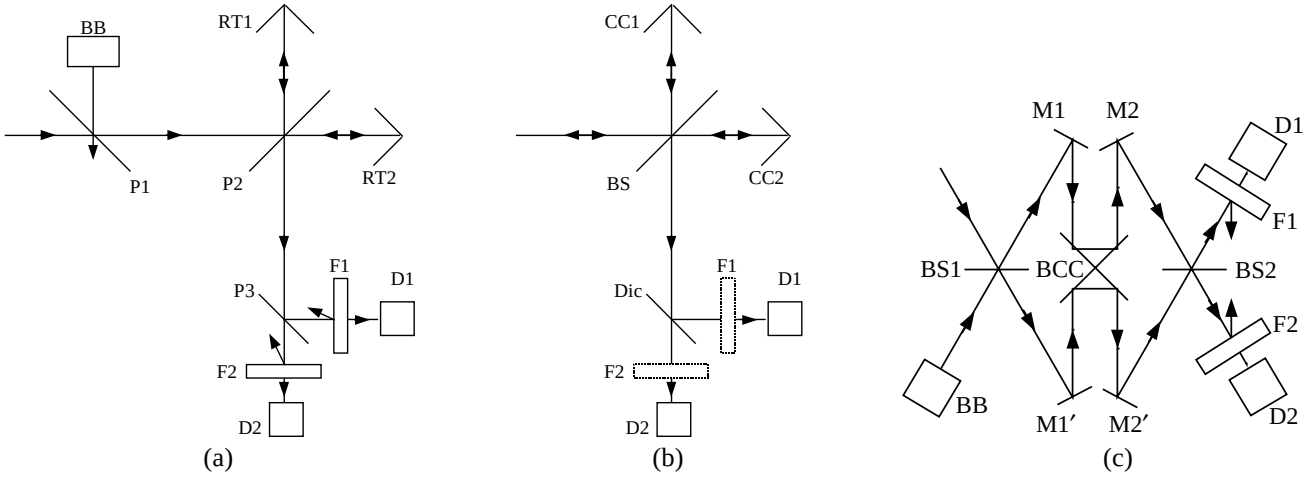

Figure 6. Three possible interferometer concepts for the SPIRE spectrometer: Martin-Puplett polarizing interferometer (a), classical Michelson interferometer (b), and Mac-Zehnder-type dual beam interferometer. BB: blackbody source, RT: roof-top mirror, P: polarizer, F: filter, D: detector, CC: corner-cube reflector (could also be mirrors or roof-tops), BS: beamsplitter, Dic: dichroic beam divider, M: mirror, BCC: back-to-back corner cubes (or roof-tops).

As a second option, we considered a simple Michelson interferometer as shown in Fig. 6 (b). This option was made possible thanks to a new development of 50/50 beamsplitters [4,6], providing greater than 90% efficiency (4RT) over the entire SPIRE band. No output polarizer is required in this case and it can be replaced with a dichroic beam divider, offering a theoretically loss-less channel separation. There is of course a 50% loss at the beamsplitter since half the incident radiation is sent back out through the telescope. Still, this configuration is twice as efficient as the previous one. Its main drawback is the lack of a second input port, required for balancing off the telescope background radiation, as will be discussed in Sec. 3.3.

The preferred solution is shown in Fig. 6 (c). Rather more complex than the former options, it provides both a second input ports and a 50% theoretical efficiency. The concept is based on a Mach-Zehnder interferometer with its arms folded in order to avoid beam shearing during scanning of the optical path difference (OPD) [5] and uses two 50/50 beamsplitters. If the detectors could be used over the entire spectral range, this concept would provide 100% efficiency, but the requirement for two separate bands imposes a 50% channel separation loss as in the Martin-Puplett case. The folding allows the optical path

of both arms to be changed simultaneously with a single scanning mechanism, hence doubling the available resolving power for a given mirror-moving mechanism. A resolving power of 1000 at 250 µm, requiring a maximum OPD of 125 mm (see Eq. 3 below), is therefore obtained with a lopsided movement from -3 mm to +31 mm. The lowest resolving powers, R = 20 to 100, are achieved using double sided scanning of ±0.6 to ±3 mm.

3.1. Beam size

Minimizing the diameter of the collimated part of the beam where the OPD scanning is performed is important to control the size of the instrument. However, by the Lagrange invariant [7], reducing the beam diameter increases the angle of off-axis beams, hence modifying the OPD. The OPD is given by the well-known relationship:

$$OPD = 2l\cos\beta\,, \tag{2}$$

where l is the distance between the mirrors in a Michelson interferometer as seen from the output port and β is the angle of an off-axis beam, see Fig. 7. The variation in OPD across the focal plane is therefore given by:

$$\Delta OPD = OPD_0(1-\cos\beta) \approx OPD_0\beta^2/2\,,$$

where OPD_0 is the axial OPD.

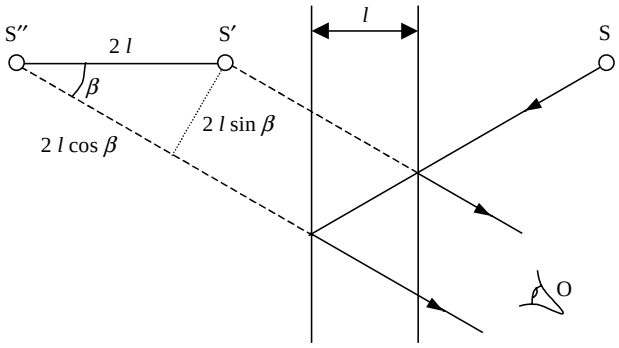

Figure 7. Construction of the relationship between OPD and field angle in the Michelson interferometer. An observer O observes the source S as reflected by each of the mirrors whose projections are separated by a distance l. The two images S′ and S″ are separeted by a distance $2l$, but their optical path difference at an angle β to the mirror normal is $2\ l\ \cos\ \beta$. The interfering beams are sheared by a distance $2\ l\ \sin\ \beta$.

In the case of a non-imaging FTS, it is common to use a circular detector of size corresponding to a change in OPD of half a wavelength, λ. This gives a slight smearing of the interferogram hence a small loss of contrast at large path differences, an effect similar to apodization. The maximum OPD required to obtain a resolving power R is given by:

$$R = 2OPD_{\max}/\lambda\,, \tag{3}$$

and so the angular limit of a classical FTS is usually expressed as:

$$\beta < \sqrt{2/R}\,. \tag{4}$$

In the case of an imaging FTS, we must consider an off-axis pixel centred at β of width $\Delta\beta$. The local variation of OPD is obtained by differentiating Eq. 2:

$$dOPD/d\beta = 2l\sin\beta\,, \tag{5}$$

and the variation in OPD across the detector pixel is therefore:

$$\Delta OPD = OPD_0\sin\beta\,\Delta\beta \approx OPD_0\beta\,\Delta\beta\,. \tag{6}$$

Hence, for a given detector width and assuming the same half-wavelength criterion as in the classical case, the angular limit may be expressed as:

$$\beta < 1/(R\,\Delta\beta)\,. \tag{7}$$

It is interesting to note that the same results may be obtained by considering the shear of the interfering beams rather than the change in OPD. The two source images shown in Fig. 7 may be considered as the sources in Young's experiment, projecting a fringe pattern onto the detection plane. A pixel must be smaller than the local fringe frequency in order to detect a signal.

Applying the Lagrange invariant, we may express the angle of a beam from the edge of the FOV as:

$$\beta = \frac{FOV}{2}\frac{D}{d}\,, \tag{8}$$

where D is the entrance pupil diameter and d is the diameter of the collimated beam within the interferometer. Assuming feed-horn detectors with aperture diameter $2F\lambda$, the angular extent of the detector as seen from the interferometer is $\Delta\beta = 2\lambda/d$, and so, substituting Eq.8 into Eq. 7 and solving for d we get:

$$d > \sqrt{R\lambda D\ FOV}\,. \tag{9}$$

For a resolving power of 1000 at 250 μm, a telescope entrance pupil of 3300 mm, and a FOV of 2.6′, the interferometer beam should therefore be greater than 25 mm. To leave some extra margin, our interferometer is designed around a beam of diameter 30 mm.

3.2. Optical design

One of the difficulties encountered in the optical design of the interferometer concept of Fig. 6 (c) was the long distance between separation (at BS1) and recombination (at BS2) of the beams. Due to the FOV dependent beam spread calculated by Eq. 8, the size of the beam splitters and collimating and camera optics became prohibitive. Also, it was difficult to find space for the scanning mechanism. To improve the situation it was decided to move collimator and camera optics to within the interferometer by making the four mirrors M1, M2, M1′, and M2′ of Fig. 6 (c) powered. This is not without disadvantages, since at non-zero OPD, the two arms do not see the same optical system. A differential aberration analysis is therefore necessary. Keeping to a strict scheme of symmetry ensures minimal aberrations in the system, and the only residual aberration of some concern is differential distortion giving a lateral separation between the images of a point source at the edge of the FOV. The induced contrast reduction is not negligible but small compared with other sources, notably alignment tolerances, see Sec. 4.

Figure 8 shows the ray diagram of the upper half of the spectrometer. The lower half has the same optical design. After reflection from the common mirrors M3, M4, and M5, the spectrometer beam is picked off by the toric M6s and sent out of the plane of the photometer system. The flat M7s redirects it into a parallel plane, separated by 170 mm from the photometer plane. The input relay mirror (Rin) focuses the beam to an intermediate image plane located just after the first beam splitter, after which the beam is collimated (Coll) and sent vertically towards the corner cube assembly. The corner cube, modelled by non-sequential raytracing, shifts the beam and sends it up towards the camera mirror (Cam). Symmetrical with the collimator, the camera focuses the beam to an image plane just before the output beam splitter. The output relay mirror (Rout) focuses the beam onto the detector arrays. To accommodate the components within the available volume, a fold mirror is needed to take the beam out of the plane again. The input and output relays are toric in order to control astigmatism and image anamorphism. A slight assymmetry in the input and output relays is introduced in order to adjust the final focal ratio. The collimator and camera mirrors are currently parabolic, but it appears possible to make them spherical without loss of performance.

A pupil image is located near the final fold mirror, making this a convenient place for the entrance hole in the 2K enclosure. This pupil moves as the OPD changes, however, so it is not appropriate for a limiting cold stop. Instead, a limiting aperture is placed in another pupil image at 4 K located between M6s and M7s.

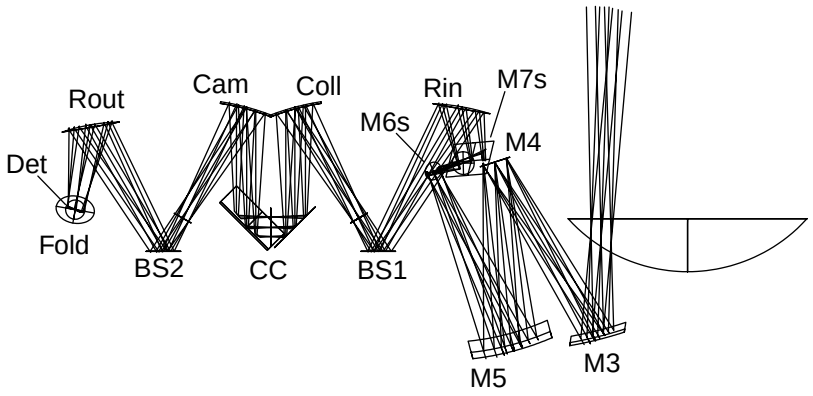

Figure 8. Raytracing diagram of the upper half of the SPIRE spectrometer. The symmetrical lower half is generated by reflection about the plane containing the two beam splitters.

Figure 9 shows spot diagrams for the spectrometer. Clearly not quite as good as those of the photometer (Fig 4), they reflect the image quality in the intermediate focal plane at M6s. Since the planar symmetry is lost, it is very difficult to improve on this. Still, the astigmatism has been brought to zero at the centre of the FOV and a good balance of aberrations over the rest of the FOV has been achieved by introducing a 3.8° rotation of the output relay mirror around its normal. The worst rms wavefront error is 6.6 microns, giving a Strehl ratio at 250μm of 0.97. Apart from a slight rotation, the image suffers from a distortion of up to 9″, corresponding to 6% of the FOV diameter.

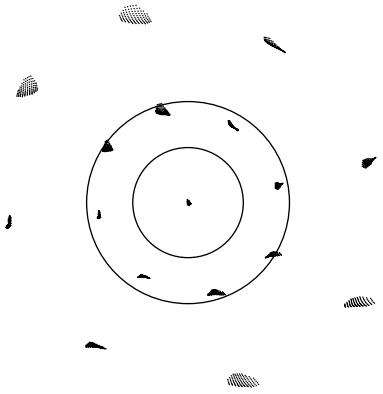

Figure 9. Geometric spot diagrams at the centre, half field, and full field of the 2.6′ diameter spectrometer FOV. The spots are plotted in their actual positions and to scale. The concentric circles around the central spot have diameters 3.7 and 6.7 mm indicating the Airy disk size at 300 and 550 μm, respectively. With a maximum RMS wavefront error of 6.6 μm, the theoretical Strehl ratio is better than 0.97 anywhere in the FOV at 250 μm. Distortion corresponding to 9″ or 6% of the FOV diameter is observed. The average focal ratio is F/4.9.

3.3. Jitter noise

One of the most critical aspects of the FTS design is the control of sampling jitter, mainly because of the large telescope background. The weak astronomical signal under study is superimposed on the much stronger black-body radiation of the telescope primary and secondary mirrors, assumed to be at a temperature of 80K and having a total emissivity of 4%. The photon noise of this background sets the ultimate detection limit of the instrument, to which the performance requirements of the detector are also adjusted. Any jitter-induced noise must be kept below this limit. The telescope background represents some 6 pW per detector in the short-wavelength (200-300 μm) spectrometer band. For a detector bandwidth of 20 Hz, this gives a ratio of background signal to background noise of 20,000 in the detected interferogram. Parseval's theorem implies that the noise power in the spectral domain is equal to the noise power in the interferogram domain. For an interferogram of length OPD_{max}, the spectral noise is therefore proportional to $\sqrt{OPD_{max}}$, and hence, by Eq. 3, to $\sqrt{R}$.

Jitter produces errors in the interferogram proportional to the local slope of the interferogram. The high background level creates a strong central peak with large slopes near the central maximum. This results in a slowly varying, undulating error in the spectrum. Since the central maximum is the same for both high and low resolution spectra, the jitter-induced spectral noise is invariant with resolving power. Simulations have shown that with a jitter specification of 0.1 μm, the spectral noise is about 20 times larger than the background photon noise at a resolving power of 20.

While improving the jitter performance beyond 0.1 µm appears exceedingly difficult, the dual input design allows another approach to this problem. In the same way that the two outputs are complementary, the two inputs have complementary sensitivities. By placing a source at the second input port exactly matching the spectral intensity of the first port, the resulting interferogram can be reduced to zero. Note that the detected power doubles, however, so the price to pay for this background nulling is a loss of $\sqrt{2}$ in effective signal-to-noise ratio. Exact knowledge of the telescope temperature and emissivity will not be available until after launch, so perfect nulling may be difficult to achieve. However, providing a source with adjustable temperature, it will be possible to reach the 95% reduction of the central maximum required to achieve background limited observations at the lowest resolving power.

For the position measurement system, a Heidenhain LIP interferential linear encoder [8] is preferred over a linear variable differential transformer (LVDT) transducer for its better accuracy. Cryogenic tests [9] indicate that this type of transducer may be used at liquid helium temperatures with only minor modifications to the optical head.

4. ALIGNMENT

Alignment of the SPIRE instrument will be performed according to a philosophy based on high-precision machining and pre-assembly 3D measurements, and a program of optical alignment checks during and after assembly. Nominally, no adjustments will be necessary, but if a serious misalignment is detected, its compensation will be possible by re-machining of certain mirror stands. Alignment of the instrument with respect to the telescope axis and pupil will be performed using a FIRST optical bench simulator consisting of a set of reference mirrors accurately located with respect to the instrument interface points. Verification of image quality and internal alignment stability will be effectuated using a set of alignment tools (sources, reticules, theodolites, …) mounted in strategic positions in the optical train (object plane, cold stop, image plane).

An optical sensitivity study shows that with an alignment tolerance of 0.1 mm and 1′ applied to all the mirrors in the photometer, the alignment-related relative pupil displacement (Sec. 2) will be less than $\Delta R/R_I = 4.1\%$. This compares favourably with the contribution from telescope alignment erros, budgeted to $\Delta R/R_T = 6.1\%$ [10], and the theoretical design contribution of $\Delta R/R_D = 5\%$ (Sec. 2). The total instrument budget is estimated by square-summing of the random alignment errors and summing of the deterministic design error:

$$\Delta R / R = \sqrt{\Delta R / R_I{}^2 + \Delta R / R_T{}^2} + \Delta R / R_D , \tag{10}$$

giving a total of 12.4%. According to Eq. (1), this gives a loss of 25% in telescope collecting area for the case of an undersized pupil.

For the spectrometer, the predominant alignment criterion is interferometer contrast, calculated from the misalignment-induced lateral separation of the interfering images using the van Zittert-Zernike theorem [11]. Note that this only concerns mounting tolerances of the fixed optical components within the interferometer (beamsplitters and collimator/camera mirrors) since the interferometer setup of Fig. 6 (c) with back-to-back corner cube reflector leaves the interferogram contrast insensitive to errors in the scanning movement. Again, tolerances of 0.1 mm and 1′ have been found appropriate, offering a contrast in the interferogram of 87%. Including mirror surface quality and differential aberrations (Sec. 3.2), a total contrast greater than 80% is expected.

Errors in the scanning movement have no influence on contrast thanks to the use of back-to-back corner cubes. However, lateral movements induce a shift in the output pupil. The shift is identical for both arms, so no shear occurs, but care must be taken to avoid vignetting. As long as the movement stays within a few tenths of a millimeter, this has no importance. More of a concern are the effects on the position transducer, for which tolerances of the order of 0.1 mm and 1′ are again required. The separation of the transducer from the optical beam imposes an even more stringent tilt tolerance for the carriage mechanism since tilting the mechanism translates into a carriage position error proportional to the distance between the measurement axis and the corner cube axis. In our system this distance is about 30 mm, hence, since the position accuracy is required to be 0.1 µm, the tilt tolerance in the plane containing the two axes is about 1″. This is a great challenge for the FTS scanning mechanism.

5. CONCLUSION

We describe the optical design of the SPIRE instrument and discusse its main design constraints. The seven-mirror photometer design is seen to consist of a three-mirror fore optics shared with the spectrometer, a field mirror, and a three-mirror Offner relay. ±2′ chopping and ±30″ beam steering is provided, and a well corrected pupil image is located at the instrument cold stop. The final image offers a near-perfect, low distortion 4′ x 8′ FOV projected onto three detector arrays via dichroic beam dividers and fold mirrors.

A Mach-Zehnder-type imaging FTS based on 50/50 beam splitters provides variable resolving power ranging from 20 to 1000. The concept was chosen for its high efficiency and dual input configuration, allowing the background compensation required to eliminate jitter noise. The beam diameter is minimized according to imaging FTS theory, and practical implementation of the design is facilitated by the use of powered mirrors within the interferometer.

Alignment tolerances of 0.1 mm and 1′ ensures acceptable performance of the instrument, both with respect to pupil postion in the photometer and fringe contrast in the spectrometer. Image quality is insensitive to this level of alignment. The alignment strategy is based on pre-integration 3D metrology and optical tests during and after integration. Errors may be compensated by re-machining strategic mirror mounts.

REFERENCES

1. M. J. Griffin, B. M. Swinyard, L. G. Vigroux, "SPIRE instrument for FIRST", Proc. SPIE **4013** (this volume), Munich, 27-31 March (2000).
2. M. E. Caldwell, B. M. Swinyard, A. Richards, "Beam pattern (diffraction) aspects in design of the SPIRE instrument", Proc. SPIE **4013** (this volume), Munich, 27-31 March (2000).
3. D. Dilworth, *The SYNOPSYS lens design program*, http://www.gwi.net/OSD/.
4. B. M. Swinyard, P.A. Ade, M. J. Griffin, P. A. Hamilton, K. Dohlen, J.P. Baluteau, D. Pouliquen, D. Ferand, P. Dargent, G. Michel, J. Martignac, L. Rodriguez, D. E. Jennings, M. E. Caldwell, A. G. Richards, "FIRST-SPIRE spectrometer: a novel imaging FTS for the submillimeter", Proc. SPIE **4013** (this volume), Munich, 27-31 March (2000).
5. D. H. Martin, "Polarizing (Martin-Puplett) interferometric spectrometers for the near- and submillimetric spectra", Infrared and millimeter waves **6**, pp. 65-148 (1982).
6. P. A. R. Ade, P. Hamilton, D. A. Naylor, "An Absolute Dual Beam Emission Spectrometer", Fourier Transform Spectroscopy: New Methods and Applications, OSA, 90 (1999).
7. W. T. Welford, *Aberrations of optical systems*, Adam Hilger, Bristol (1989).
8. *Exposed linear encoders*, http://www.heidenhain.com/Products/ExposedLinear/lip.htm
9. G. Michel and J. Martignac (private communication).
10. *FIRST alignment plan*, ESA document PT-PL-02220, 9/5/1996.
11. D. K. Lambert, P. L. Richards, "Martin-Puplett interferometer: an analysis", Applied Optics **17**, pp. 1595-1602 (1978).